



Cite this: *J. Mater. Chem. A*, 2015, 3, 24095

Flower-to-petal structural conversion and enhanced interfacial storage capability of hydrothermally crystallized MnCO_3 via the *in situ* mixing of graphene oxide†

Shiqiang Zhao, Fan Feng, Faqi Yu and Qiang Shen*

Graphene oxide (GO) possesses high electron conductivity and good chemical-binding ability and thus can be used as a multifunctional additive for the preparation and application of electrode materials. As for the hydrothermal crystallization of MnCO_3 herein, the absence of GO causes the formation of MnCO_3 flower-like architectures composed of secondary spindles, while the presence of GO induces the flower-to-petal structural conversion and results in MnCO_3 spindle-GO composites. When applied as Li-ion battery anodes, the composite electrode delivers an initial coulombic efficiency (CE) of 71% and a reversible capacity of 1474 mA h g^{-1} in the 400th cycle, much higher than those of MnCO_3 flowers (the initial CE $\sim 58\%$, the 400th capacity $\sim 1095 \text{ mA h g}^{-1}$) operated under the same conditions. In particular, the combination of discharging behavior and its differential capacity profile has been successfully used to estimate the interfacial contribution fraction (42%) of the whole reversible capacity (*i.e.*, 1474 mA h g^{-1}) enhanced by the *in situ* mixing of 8.3 wt% GO.

Received 15th September 2015

Accepted 30th October 2015

DOI: 10.1039/c5ta07390a

www.rsc.org/MaterialsA

1. Introduction

Owing to the well-known advantages of high energy density, long lifespan and good environmental benignity, rechargeable lithium ion batteries (LIBs) have obtained a great commercial achievement in portable electronics. However, the low theoretical capacities and high cost of commercial electrode materials can hardly satisfy the ever-growing demands of large-scale high-energy applications such as electric vehicles and smart grids.^{1,2} Therefore, the research and development of high-capacity electrode materials with excellent cycling stability and high-rate performance is of crucial importance presently.^{3–8}

In recent years, transition metal carbonates (TMCs) have been widely investigated as a new kind of available high-capacity anode materials for LIBs, which could exhibit a long-term practical reversible capacity higher than 1000 mA h g^{-1} .^{9–16} On the one hand the traditional conversion reaction of $\text{MCO}_3 + 2\text{Li} \leftrightarrow \text{Li}_2\text{CO}_3 + \text{M}^0$ (*e.g.*, $\text{M} = \text{Co}, \text{Fe}$ or Mn) relates to

a theoretical capacity of about 450 mA h g^{-1} , and on the other hand the further and partly electrochemical catalytic conversion mechanism of intermediate Li_2CO_3 (*i.e.*, $\text{Li}_2\text{CO}_3 + (4 + 0.5x)\text{Li} \xrightarrow{\text{M}^0 \text{ nanoparticles}} 3\text{Li}_2\text{O} + 0.5\text{Li}_x\text{C}_2$; $x = 0, 1$ or 2) accounts for the ultrahigh practical capacity of TMCs to a great extent.^{17–22} As for the reversible conversion of intermediate Li_2CO_3 to low-valence carbon-containing substances (*i.e.* C^{2+} , C^0), Zhou *et al.* deduced this according to the C1s binding energy of the discharged CoCO_3 mainly.¹⁷ Afterwards, Zhang *et al.* confirmed the transition from CoCO_3 to Li_2CO_3 and then to Li_xC_2 ($x = 0, 1, 2$) and Li_2O using the *ex situ* Fourier-transformed infrared (FTIR) spectra of discharged CoCO_3 -polypyrrole composites.¹⁸ Recently, Wang *et al.* clarified that intermediate Li_2CO_3 could indeed be converted into Li_2C_2 and/or Li_2O by serial analytical methods such as cyclic voltammetry, spectroscopy (*i.e.* Raman and FTIR spectra) and transmission electron microscopy analyses.¹⁹ Among these TMCs, manganese carbonate (MnCO_3) is one of the hottest target compounds because of both its facile hydrothermal synthesis regarding the further oxidation of iron(II) species and its nontoxicity, low cost and abundant resources compared with elemental cobalt.^{22–29} Also, similar to other TMCs, the large volume change of crystalline MnCO_3 as well as its inherent drawback of low electron conductivity substantially needs to be overcome for the high-capacity feature of MnCO_3 -based electrodes.^{30–33}

According to recent literature reports,^{22,24,26,29,34} two progresses have been well demonstrated: (i) the controllable

Key Laboratory for Colloid and Interface Chemistry of Education Ministry, School of Chemistry and Chemical Engineering, Shandong University, Jinan 250100, PR China. E-mail: qshen@sdu.edu.cn; Fax: +86-531-88564464; Tel: +86-531-88361387

† Electronic supplementary information (ESI) available: Structural characterization of the MnCO_3 spheres obtained in the absence of both CA and GO, Raman spectra of MnCO_3 spindle-GO composites, HRTEM images of the intermediates precipitated from the hydrothermal crystallization system of MnCO_3 spindle-GO composites, and discharge profiles and corresponding dQ/dV curves of MnCO_3 flowers and MnCO_3 spindle-GO composites. See DOI: 10.1039/c5ta07390a

preparation of nanostructured MnCO_3 could effectively buffer the volume change occurring during lithiation–delithiation processes and maintain the structural integrity of assembled electrodes; (ii) the *in situ* and homogeneous mixing of conductive additives (e.g. graphene or carbon nanotube) into nano-crystalline MnCO_3 could further achieve the excellent mechanical flexibility, superior electrical conductivity and high thermal and chemical stabilities of active substances. Therein, the large specific surface area of active substances and the corresponding interfacial lithium storage capability of the nanostructured electrode should not be omitted. Compared with the theoretical capacity of an active substance, the interfacial lithium storage contribution occurring at the phase interfaces of electrodes can be referred to as an “extra” part of the whole capacity.^{35–40} Presently, much effort has been devoted to improve the lithium storage capability of nanostructured electrodes and a sufficient prerequisite to observe interfacial storage behavior is the large specific surface area of active substances.^{41–44} As far as we know, the high-capacity mechanism of nanostructured TMCs is still ambiguous, let alone the unexplained interfacial storage capability involved therein.

In this paper, the absence and presence of graphene oxide (GO) in the hydrothermal crystallization system of manganese acetate ($\text{Mn}(\text{Ac})_2$), citric acid (CA) and ammonium bicarbonate (NH_4HCO_3) were comparatively conducted, resulting in flower-like hierarchical structures composed of crystalline MnCO_3 nanospindles and their nanocomposites with additive GO, respectively. Considering the functions of additive GO for the modified structural and electrochemical properties of crystalline MnCO_3 , the resulting MnCO_3 spindle–GO composites unexpectedly exhibit an ultrahigh interfacial storage capability compared with the unmixed MnCO_3 hierarchical flowers. On the principle of the conversion reaction of TMCs reported in the literature, the combination of the voltage profile and its differential result was used to estimate the interfacial storage capability of carbonate-based active substances for the first time, proving the interfacial lithium storage effectiveness of mixing GO for LIB anodes.

2. Experimental

2.1 Materials preparation

All the chemicals are of analytic grade and ultrapure water (18.2 M Ω cm) was used throughout the solution preparation. A facile hydrothermal crystallization method was adopted for the preparation of MnCO_3 flowerlike hierarchical structures, shown below. Firstly, solid-state manganese acetate tetrahydrate ($\text{Mn}(\text{CH}_3\text{COO})_2 \cdot 4\text{H}_2\text{O}$, 1 mmol) and citric acid monohydrate (CA, 1 mmol) were dissolved in 30 mL water and then aqueous ammonium bicarbonate NH_4HCO_3 (1 M, 10 mL) was dropwise added under vigorous stirring at room temperature. Secondly, the resulting suspension was transferred into a 50 mL Teflon-lined autoclave, sealed and allowed to stand still in a thermostatic chamber at 160 °C for 15 h. Finally, the autoclave was cooled down to room temperature, and the precipitates were collected by centrifugation, and then washed with ultrapure

water and absolute alcohol 3 times in sequence and then dried at 80 °C for 10 h.

In the laboratory, GO was freshly prepared from graphite powder using a modified Hummers method, and after the hydrothermal treatment the partial reduction features of GO had been clearly described in one of our previous results.⁴⁵ To obtain the target products of MnCO_3 spindle–GO composites, aqueous GO suspension (1 g L^{−1}) was freshly prepared and then the above-mentioned procedure was used by substituting the 30 mL GO suspension for 30 mL ultrapure water.

To illustrate the formation mechanism of MnCO_3 flowerlike hierarchical structures and the influence of added GO, time-dependent experiments were conducted and the hydrothermal incubation times were selected to be 1, 2, 5 and 10 h.

2.2 Material characterization

Scanning electron microscopy (SEM, JEOL JSM-6700F) measurements were performed using a field emission source with an accelerating voltage of 15 kV. X-ray diffraction (XRD, Rigaku D/max-2400) tests were conducted using Cu-K α radiation ($\lambda = 1.5406$ Å, 40 kV, 120 mA), 0.08° step (25 s) and the 2 θ range of 10–80°. Thermogravimetric analysis (TGA) and differential scanning calorimetry (DSC) were performed under air atmosphere with a heating step of 10 °C min^{−1} from room temperature to 900 °C. Brunauer–Emmet–Teller (BET) isotherms and specific surface area (*i.e.*, BET surface area) were obtained using a Micromeritics ASAP 2020 sorptometer, and the corresponding pore size distributions were derived using the analytical method of Barrett–Joyner–Halenda (BJH). Samples were dispersed in ethanol by ultrasonication and then deposited on a carbon film supported by a copper grid prior to transmission electron microscopy (TEM) and high-resolution TEM (HRTEM) measurements on a JEM 2100 microscope (200 kV).

2.3 Electrochemical measurements

After dispersing the as-prepared MnCO_3 sample, acetylene black and sodium alginate at a weight ratio of 7 : 2 : 1 in ultrapure water, the resulting homogeneous slurry was pasted onto a pure copper foil and dried at 80 °C for 12 h. And then, the foil was cut into discs (12 mm in diameter) and used as working electrodes with a loading density of 1.5 ± 0.2 mg cm^{−2}. Lithium metal, copper foil, Celgard 2300 microporous membrane and commercial LBC 305-01 LiPF₆ solution (Shenzhen Xinzhou-bang) were used as the counter electrode, current collector, separator and electrolyte, respectively. CR2032-type coin cells were assembled in an argon-filled glovebox.

Cyclic voltammetry (CV) curves were collected on an LK 2005A Electrochemical Workstation (Tianjin Lanlike) at 0.1 mV s^{−1} within the potential window of 0.01–3.0 V (*vs.* Li/Li⁺ and hereafter). Galvanostatic cycling tests were conducted on a LAND CT2001A system (Wuhan Landian) in the voltage range of 0.01–3.0 V. Electrochemical impedance spectroscopy (EIS, Materials Mates 510, Italia) measurements were carried out within the frequency range of 0.1 MHz to 0.01 Hz.

3. Results and discussion

3.1 Flower-to-petal structural conversion

In the absence of additive GO, the 15 hour hydrothermal reaction of $\text{Mn}(\text{Ac})_2$, citric acid (CA) and NH_4HCO_3 at 160°C results in MnCO_3 flowerlike hierarchical structures composed of spindle-shaped petals with an average length of $1.2 \pm 0.2\ \mu\text{m}$ (Fig. 1a and the inset). As demonstrated previously,¹³ prior to the addition of NH_4HCO_3 a strong electrostatic interaction between Mn^{2+} ions and crystal-modifier CA may manipulate the oriented attachment of tiny building blocks for the formation of secondary spindles, which could be deduced in contrast to the hydrothermal crystallization of MnCO_3 spheres in the absence of CA (Fig. S1-a†). And then, the further aggregation of these nanospindles could be attributed to energy minimization.

When the multifunctional additive GO was added into this hydrothermal crystallization system, the well-dispersed nanosheets of GO could prevent the interlayer diffusion of carbonate ions and the surface-rich functional groups (*e.g.*, $-\text{OH}$ and $-\text{COOH}$ groups) of GO may act as active sites for nucleation, resulting in relatively short nanospindles of crystalline MnCO_3 with an average length of $590 \pm 50\ \text{nm}$ (Fig. 1b). Thereafter, the *in situ* mixing of GO nanosheets could further hinder the agglomeration of MnCO_3 nanospindles through their hydrothermally cross-linking functions (an inset in Fig. 1b), that is, MnCO_3 nanospindles mostly localize on the surfaces of GO nanosheets and the mixing of GO ultrathin nanosheets could be proved by the combined results of Raman measurements and TEM observations (Fig. S2 and S3†).

In the absence or presence of GO, the as-obtained precipitates exhibit patterns in agreement with the standard XRD data

of phase-pure rhodochrosite ($a = 4.790\ \text{\AA}$, $c = 15.684\ \text{\AA}$, JCPDS No. 44-1472), shown in Fig. 1c. Therein, the cross-linking of GO with inorganic carbonates comparatively exerts almost no influence on the crystal phase of MnCO_3 . Even in the 2θ range of $8\text{--}80^\circ$ almost no XRD signals from GO nanosheets are identified for the MnCO_3 spindle-GO composites, suggesting that the surface deposition of crystalline carbonates can suppress the further stacking of sheet-like GO.

An integrative technique of TGA and DSC was used to estimate the contaminant amount of additive CA and/or GO in these products, considering the complete transformation of additive CA or GO into gaseous species (Fig. 1d and S1b-d†). Moreover, if contaminants CA and GO exert no influence on the chemical decomposition of crystalline MnCO_3 , the mixing amount of additives in MnCO_3 flowerlike hierarchical structures (*i.e.*, additive CA) and MnCO_3 spindle-GO composites (*i.e.*, additives CA and GO) could be estimated to be ~ 3.1 and $11.4\ \text{wt\%}$, respectively. Herein it should be emphasized that only the mixing of GO (*i.e.*, $8.3\ \text{wt\%}$) was used to assay its effect on the structural and electrochemical properties of hydrothermally crystallized MnCO_3 in context.

To investigate the hydrothermal formation process of crystalline nanostructures, time-dependent experiments of the MnCO_3 flowers and MnCO_3 spindle-GO composites were comparatively conducted at the incubation times of 1, 2, 5 and 10 h. As shown in Fig. 2a-c, at 160°C the reaction interval of 1 h is enough for the nucleation and initial aggregation of tiny building blocks for the formation of spindle-shaped aggregates. These secondary spindles may immediately self-assemble to form flower-like hierarchical structures in the absence of GO, while these secondary particles could be stabilized by the

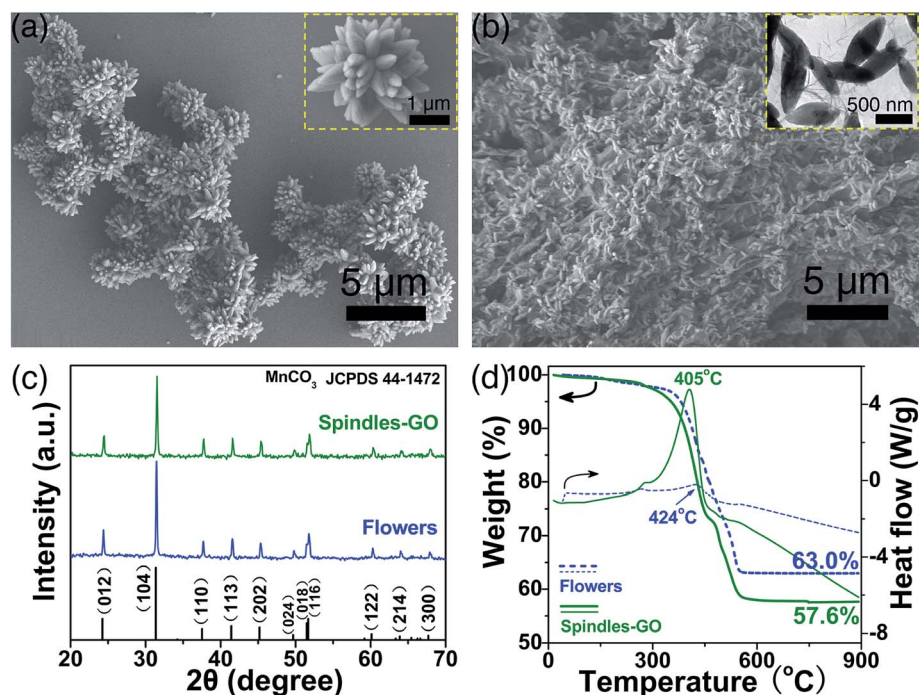


Fig. 1 (a and b) SEM images, (c) XRD patterns and (d) TGA-DSC curves of MnCO_3 flowers and MnCO_3 spindle-GO composites.

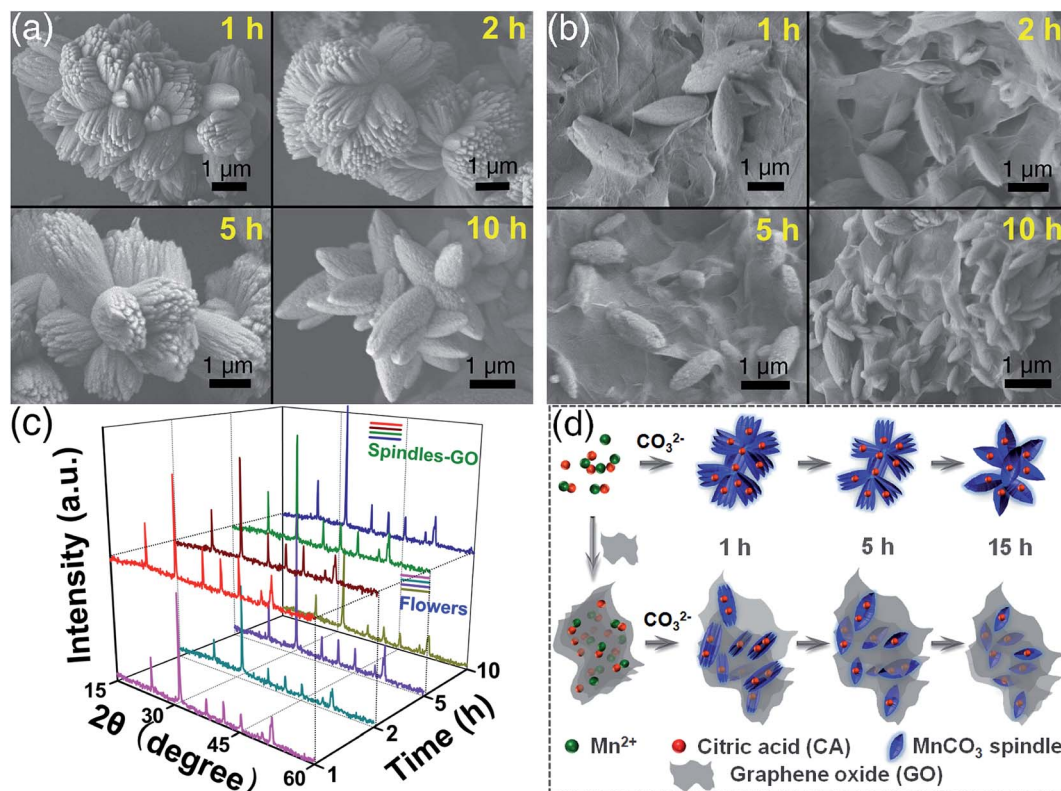


Fig. 2 (a and b) SEM images and (c) XRD patterns of the intermediates collected at the hydrothermal reaction times of 1, 2, 5 and 10 h. (d) Schematic diagram of the formation processes of MnCO₃ flowers and MnCO₃ spindle-GO composites.

addition of GO prior to the hydrothermal treatment. No matter whether additive GO was present in the hydrothermal crystallization system or not, a size-shrunk phenomenon of spindle-shaped aggregates could be clearly observed thereafter, assigned to the further aggregation of adjacent primary building blocks principally (Fig. 2a–c). Taking the average length of spindles formed in the presence of GO as an example, by statistical analysis there are 3.4 ± 0.4 , 1.6 ± 0.4 , 1.3 ± 0.3 and 0.8 ± 0.1 μm at the reaction intervals of 1, 2, 5 and 10 h, respectively (Fig. 2b).

Herein, an electrostatic interaction between the head-group of citric acid (CA) and Mn²⁺ ions should be emphasized, which cuts down the crystal-modified actions of subsequently added GO for the initial nucleation and consequent crystal growth of MnCO₃. This is the reason why only the dispersion effect of GO can be visually detected (Fig. 2b and S3†). As schematically shown in panel (g) of Fig. S3, † the extrusion of additive CA may also occur along with the further aggregation of tiny MnCO₃ nanoparticles. Therefore, the effect of *in situ* added GO on hydrothermally crystallized MnCO₃ could be artificially described as the simple “exfoliation” of flowers into spindle-shaped petals, which is shown in Fig. 2d schematically.

3.2 Enhanced interfacial storage capability

Using MnCO₃/Li cell models, the electrochemical properties of the as-obtained MnCO₃ spheres, flowers and MnCO₃ spindle-

GO composites were comparatively examined (Fig. 3 and S4†). Owing to both the relatively small particle size of MnCO₃ spindles and the effective mixing of GO, the cycling stability and rate performance of MnCO₃ spindle-GO composites are better than those of MnCO₃ flowers (Fig. 3a and b). For instance, at 200 mA g⁻¹ the reversible capacity of MnCO₃ spindle-GO composites in the 60th discharge-charge cycle is 1026 mA h g⁻¹, while that of MnCO₃ flowers is only 720 mA h g⁻¹ (Fig. 3a). Even at a low current rate (*i.e.*, C-rate) of 100 mA g⁻¹ or a high C-rate of 2000 mA g⁻¹, in each cycle the observed discharge capacity of the GO-mixed composite electrode is always higher than that of the “pure” MnCO₃ anode (Fig. 3b). Prior to a long-term cycling test at 1000 mA g⁻¹, the working electrode was initially activated at 100 mA g⁻¹ for 3 discharge-charge cycles. Subsequently, the reversible capacity of MnCO₃ spindle-GO composites could stabilize at a high value of 807 mA h g⁻¹, while that of MnCO₃ flowers increases at first and then reaches a low value of ~579 mA h g⁻¹ from the 4th to 200th cycles (Fig. 3c). Also in Fig. 3c, when the C-rate returns back from 1000 to 100 mA g⁻¹, the GO-mixed composite electrode interestingly exhibits an upward trend of reversible capacity for the further galvanostatic cycling in contrast to the “pure” MnCO₃ electrode, reaching an ultra-high value of ~1474 mA h g⁻¹ in the 400th cycle.

At 200 mA g⁻¹ the 1st and 60th voltage profiles of the two electrodes are comparatively shown in Fig. 3d. Therein, each of the initial discharging curves gives a low irreversible voltage plateau at ~0.3 V, corresponding to both the first

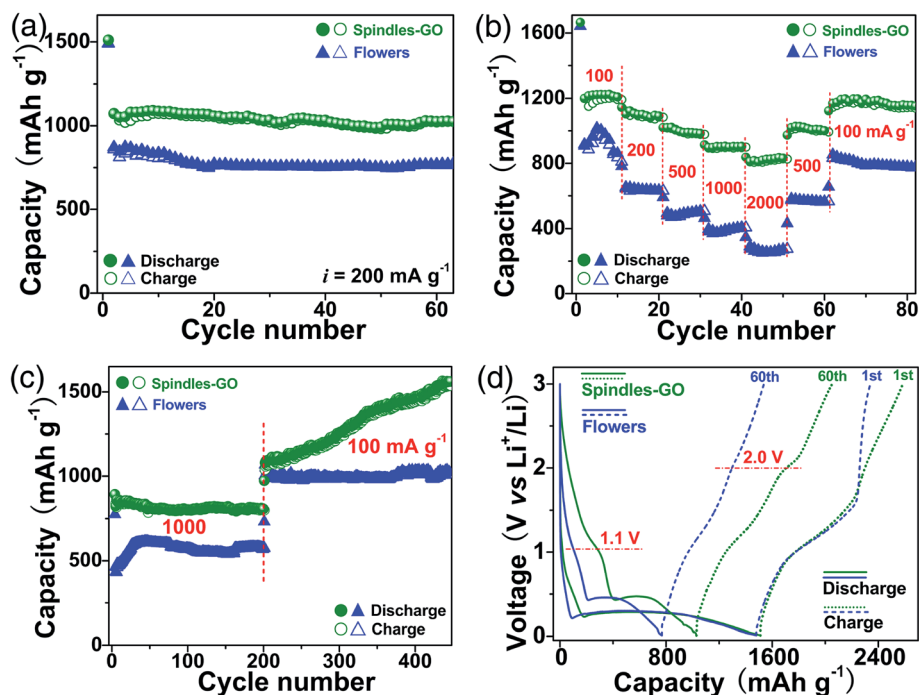


Fig. 3 (a) Cycling stabilities, (b) rate performances, (c) long-term cycling tests and (d) voltage profiles of the comparative electrodes of MnCO₃ flowers and MnCO₃ spindle-GO composites.

electrochemical lithiation of crystalline MnCO₃ and the formation of solid-electrolyte interphase (SEI) layers.^{26,28,29} Although each of the initial charging curves exhibits a similar voltage plateau at ~1.2 V, the GO-mixed composite and the “pure” MnCO₃ electrode distinguishingly give a coulombic efficiency of ~71% and 58%, respectively. As for the 60th voltage profiles shown in Fig. 3d, the lithiation of MnCO₃ gives a “new” voltage plateau at a high voltage of ~1.1 V, and the delithiation of MnCO₃ correspondingly shows the “new” high-voltage plateau at ~2.0 V no matter whether additive GO is present or not. Therefore, the effective mixing of conductive GO does not exert any influence on the lithiation–delithiation mechanism of anode active substance MnCO₃ but may improve its interfacial activity and/or electrochemical reversibility.

A reversible electrochemical reaction process of MnCO₃ towards metallic Li can be generally illustrated by all the redox peaks appearing in CV profiles. As representatively shown in Fig. 4a, at 0.1 mV S⁻¹ the partly magnified CV curve of MnCO₃ flowers in the 10th cycle visually exhibits a pair of anodic/cathodic peaks of MnCO₃ at ~1.98/1.05 V, and by comparison the relatively strong CV peak intensities of the active substances in GO-mixed composites could ensure the improved interfacial activity and/or electrochemical reversibility therein (Fig. 4a and S5†). Herein, we would like to cite the CV results of MnCO₃ and manganese oxides (*e.g.* MnO and Mn₂O₃) reported in the literature;^{29,44,46–49} cathodic peaks at ~1.05 and 0.25 V may be ascribed to the reduction of Mn³⁺ to Mn²⁺ and then to Mn⁰, and the corresponding anodic peaks at ~1.16 and 1.98 V relate to the reverse two-step oxidation. That is, this may deal with the gradual oxidation of the bivalent M²⁺ in MCO₃ (Fig. S5†) and

could be further proved by a possible origination of the extra Li-storage capacity of the FeCO₃ anode reported previously.²⁰ Importantly, this coincides well with the “new” voltage plateaus appearing at ~1.1 and 2.0 V in the 60th discharge–charge profile as shown in Fig. 3d.

In Fig. 4b, N₂ adsorption–desorption isotherms of both MnCO₃ flowers and MnCO₃ spindle-GO composites could be approximately classified as type IV isotherms with a type H3 hysteresis loop, and the estimated specific surface area (*i.e.*, the BET surface area) of MnCO₃ GO-mixed composites (28 m² g⁻¹) is much higher than that of “pure” MnCO₃ (4 m² g⁻¹). According to their pore size distributions inserted in Fig. 4b, there are absolutely no porous characteristics for “pure” MnCO₃ flowers compared to MnCO₃ spindle-GO composites. Aside from the relatively small average particle size of MnCO₃ secondary spindles, the high BET surface area and porous feature of GO-mixed composites may be attributed to both the effective mixing of the conductive nanosheets and the relatively small particle size of primary building blocks.

In the absence or presence of GO, the Nyquist plot of a freshly assembled MnCO₃ electrode presents a depressed semicircle at high and medium frequencies, relating to the charge transfer process across the electrode surface (Fig. 4c). According to the equivalent circuit inserted in Fig. 4c, the estimated charge-transfer resistance (R_{ct}) of MnCO₃ spindle-GO composites is ~186 Ω, much lower than that of MnCO₃ flowers (*i.e.*, 469 Ω). The mixtures composed of the MnCO₃-based active substance (70 wt%), conductive agent acetylene black (20 wt%) and water-soluble binder sodium alginate (10 wt%) were unpacked from model cells cycled sixty times at 200 mA g⁻¹, and the corresponding SEM image exhibits all of them in

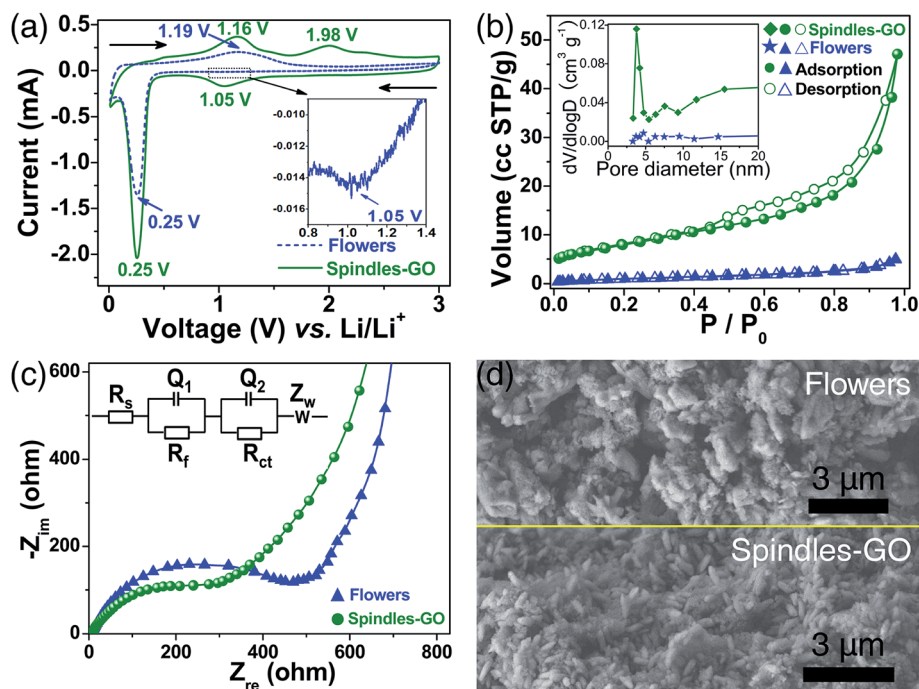


Fig. 4 (a) Representative CV curves, (b) N₂ adsorption–desorption isotherms and (c) Nyquist plots of comparative MnCO₃ flowers and MnCO₃ spindle–GO composites. (d) SEM images of the electrochemically cycled electrodes of (upper) MnCO₃ flowers and (lower) MnCO₃ spindle–GO composites, respectively.

morphology (Fig. 4d). In the upper part of Fig. 4d, a severe pulverization phenomenon of “pure” MnCO₃ flowers and secondary spindles is visually detected, but the spindle-shaped configuration of MnCO₃ obviously remains unchanged for GO-mixed composites (lower part, Fig. 4d). Thus, the mixing of GO further endues MnCO₃ spindles with an enhanced structural stability or electrochemical durability.

Unfortunately, these results of Fig. 4 still cannot account for the upward trend of the reversible capacity of the GO-mixed composite electrode shown in Fig. 3c. Herein, two aspects need to be mentioned: (i) the ultrahigh reversible capacity of the MnCO₃ spindle–GO composite anode (e.g., 1474 mA h g⁻¹, the 400th cycle, 100 mA g⁻¹) was calculated according to the total weight of GO, CA and MnCO₃ and otherwise it should be higher; (ii) even if the two-step discharging reaction consumes 7 moles of Li per mole of MnCO₃ and the estimated value of “theoretical capacity” (i.e., 1633 mA h g⁻¹) is similar to the practical ones, it still cannot explain the gradual capacity increase of MnCO₃ spindle–GO composites rather than that of MnCO₃ flowers.^{17–19} Therefore, the enhanced interfacial storage capability of additive GO should be emphasized as shown in Fig. 5 and S6† in detail.

Based on the principle of the conversion reaction mechanism of a MCO₃-based anode, three lithium storage regions might be distinguished for a discharging process in sequence:^{36,41,50} a rapid voltage decay region corresponding to the homogeneous lithium insertion into the bulk electrode (i.e., non-reactive lithium storage), an obvious voltage plateau region relating to the bulk conversion reaction (i.e., reactive lithium storage), and a slow voltage decay region dealing with the

lithium storage at particle interfaces (i.e., interfacial lithium storage). In a voltage profile, the boundaries among the three regions are generally ambiguous but can be clearly distinguished using its differential capacity (dQ/dV) curve. As shown in Fig. 5a or b, the cathodic peaks of the lithiation reaction in each dQ/dV curve correspond well with the voltage plateaus in the corresponding voltage profile, which is classified into the so-called reactive lithium storage region herein.

Three aspects should be emphasized that: (i) the so-called non-reactive lithium storage depends upon both the structural parameters (e.g., porosity) of the active substance and the operated voltage limit of the discharge–charge cycle, (ii) the reversible capacity originating from both the non-reactive and reactive lithium storage regions mainly happens within the bulk electrode and can be combined as the commonly defined bulk lithium storage capacity, and (iii) herein this partition seems to be reasonable to estimate the “extra” capacity contribution of pseudo-capacitance occurring at the interface between lithiated and delithiated phases. According to the cycling results shown in Fig. 3c, the practical lithium storage capacity (1095 mA h g⁻¹) of the “pure” MnCO₃ anode in the 400th cycle can be divided into 792 (the bulk fraction ~ 72%) and 303 mA h g⁻¹ (the interfacial fraction ~ 28%), respectively (Fig. 5a). Similarly, the 400th Li-storage capacity (1474 mA h g⁻¹) of the GO-based composite electrode can be divided into 848 (the bulk fraction ~ 58%) and 626 mA h g⁻¹ (the interfacial fraction ~ 42%), respectively (Fig. 5b).

Comparing Fig. 5a with 5b, the improved interfacial Li-storage capability of the composite electrode can be assigned to its modified structural parameters (e.g., the particle size and

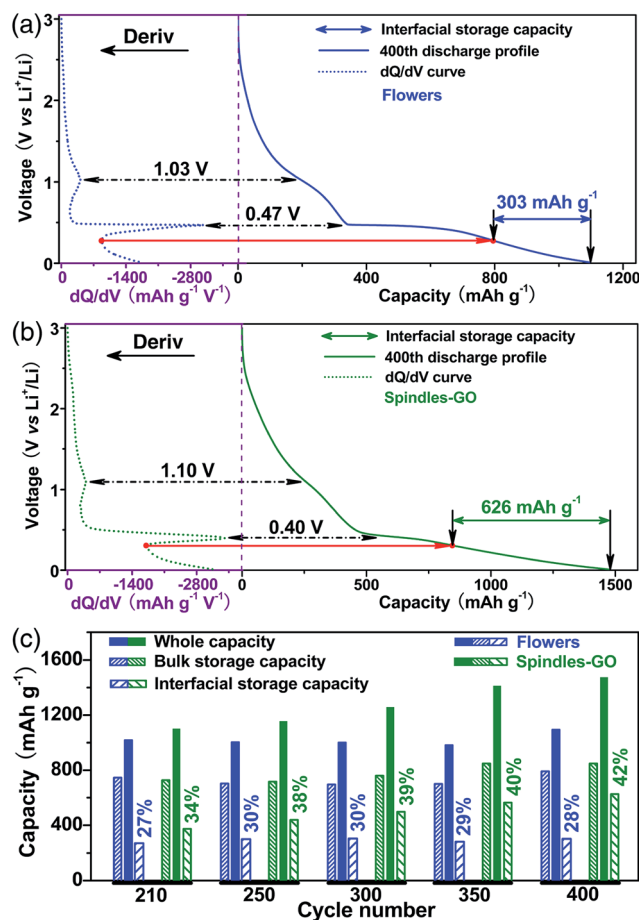


Fig. 5 (a and b) The combination of the discharging profile and corresponding dQ/dV curve of MnCO₃ flowers and MnCO₃ spindle-GO composites operated at 100 mA g⁻¹ in the 400th cycle, respectively. (c) Histograms of the comparative interfacial storage capabilities of MnCO₃ flowers and MnCO₃ spindle-GO composites in each cycle.

porosity) and/or the enhanced structural stability, while their similar bulk Li-storage capacity ($\sim 800 \text{ mA h g}^{-1}$) can be attributed to the same electrochemical reaction between MnCO₃ and metallic Li. In the 210th, 250th, 300th, 350th and 400th cycles, the electrode of MnCO₃ spindle-GO composites exhibits a gradually increasing ratio of interfacial storage capacity to the whole capacity along with the increase of the cycle number (*i.e.*, from 34% to 42%), while the “pure” MnCO₃ electrode gives an almost stable value (*i.e.*, $\sim 30\%$) under the same circumstances (Fig. 5c). Even for the previous cycling tests operated at 1000 mA g^{-1} , this phenomenon could also be detected (Fig. S6†). Compared to MnCO₃ flower-like hierarchical structures, the gradually increasing interfacial storage capacity of MnCO₃ spindle-GO composites could be attributed to both the improved conductivity and the increased BET surface area with a relatively high interfacial stability. Moreover, we would like to emphasize that this try may reveal the enhanced interfacial storage capability as one of the most important origins for the high-capacity characteristics of MnCO₃-GO nanostructured composites.

4. Conclusions

In summary, MnCO₃ flower-like hierarchical structures or MnCO₃ spindle-GO composites can be uniquely obtained from a hydrothermal crystallization system in the absence or presence of GO, and additive GO is visually functionalized as a scale-inhibiting or dispersing agent to induce the flower-to-petal conversion of crystalline MnCO₃ therein. Also, the mixing of 8.3 wt% GO could increase the specific surface area of the electrode active substance, modify the reaction reversibility of MnCO₃ towards metallic Li, decrease the charge transport resistance of the working electrode and improve the structural stability of MnCO₃ secondary spindles. Based on the long-term cycling tests of GO-mixed composites operated at 1000 and 100 mA g^{-1} alternatively, the combination of voltage profiles and corresponding dQ/dV curves could successfully estimate the bulk (57.6%) and interfacial contribution fractions (42.4%) of the whole reversible capacity (1474 mA h g^{-1} , 400th cycle, 100 mA g^{-1}) enhanced by the effective mixing of GO. That is, it is the gradually increasing interfacial Li-storage capability that reasonably explains the abnormal uptrend of reversible capacity along with the increase of the cycle number. However, future studies still need to deal with the presently unexplained interfacial storage mechanism of conductive carbon-doped TMC nanostructures.

Acknowledgements

Financial support from Beijing National Laboratory for Molecular Science and from Shandong University (2014JC016) is greatly acknowledged.

References

- 1 B. Dunn, H. Kamath and J. Tarascon, *Science*, 2011, **334**, 928.
- 2 B. Guo, X. Yu, X. Sun, M. Chi, Z. Qiao, J. Liu, Y. Hu, X. Yang, J. Goodenough and S. Dai, *Energy Environ. Sci.*, 2014, **7**, 2220.
- 3 P. G. Bruce, B. Scrosati and J.-M. Tarascon, *Angew. Chem., Int. Ed.*, 2008, **47**, 2930.
- 4 H. Jiang, Y. Hu, S. Guo, C. Yan, P. Lee and C. Li, *ACS Nano*, 2014, **8**, 6038.
- 5 S. Zhang, L. Zhu, H. Song, X. Chen and J. Zhou, *Nano Energy*, 2014, **10**, 172.
- 6 R. Lee, Y. Lin, Y. Weng, H. Pan, J. Lee and N. Wu, *J. Power Sources*, 2014, **253**, 373.
- 7 X. Sun, Y. Xu, P. Ding, G. Chen, X. Zheng, R. Zhang and L. Li, *J. Power Sources*, 2014, **255**, 163.
- 8 S. Guo, G. Lu, S. Qiu, J. Liu, X. Wang, C. He, H. Wei, X. Yan and Z. Guo, *Nano Energy*, 2014, **9**, 41.
- 9 S. Zhao, Y. Wang, R. Liu, Y. Yu, S. Wei, F. Yu and Q. Shen, *J. Mater. Chem. A*, 2015, **3**, 17181.
- 10 L. Wang, W. Tang, Y. Jing, L. Su and Z. Zhou, *ACS Appl. Mater. Interfaces*, 2014, **6**, 12346.
- 11 Y. Sharma, N. Sharma, G. Rao and B. Chowdari, *J. Mater. Chem.*, 2009, **19**, 5047.
- 12 J. Zhao and Y. Wang, *J. Mater. Chem. A*, 2014, **2**, 14947.

- 13 S. Zhao, S. Wei, R. Liu, Y. Wang, Y. Yu and Q. Shen, *J. Power Sources*, 2015, **284**, 154.
- 14 M. Garakani, S. Abouali, B. Zhang, C. Takagi, Z. Xu, J. Huang and J. Kim, *ACS Appl. Mater. Interfaces*, 2014, **6**, 18971.
- 15 F. Zhang, R. Zhang, J. Feng, L. Ci, S. Xiong, J. Yang, Y. Qian and L. Li, *Nanoscale*, 2015, **7**, 232.
- 16 G. Huang, S. Xu, Y. Yang, H. Sun, Z. Li, Q. Chen and S. Lu, *Mater. Lett.*, 2014, **131**, 236.
- 17 L. Su, Z. Zhou, X. Qin, Q. Tang, D. Wu and P. Shen, *Nano Energy*, 2013, **2**, 276.
- 18 Z. Ding, B. Yao, J. Feng and J. Zhang, *J. Mater. Chem. A*, 2013, **1**, 11200.
- 19 N. Tian, C. Hua, Z. Wang and L. Chen, *J. Mater. Chem. A*, 2015, **3**, 14173.
- 20 S. Zhao, Y. Yu, S. Wei, Y. Wang, C. Zhao, R. Liu and Q. Shen, *J. Power Sources*, 2014, **253**, 251.
- 21 Y. Zhong, L. Su, M. Yang, J. Wei and Z. Zhou, *ACS Appl. Mater. Interfaces*, 2013, **5**, 11212.
- 22 M. Gao, X. Cui, R. Wang, T. Wang and W. Chen, *J. Mater. Chem. A*, 2015, **3**, 14126.
- 23 M. Aragon, C. Perez-Vicente and J. Tirado, *Electrochem. Commun.*, 2007, **9**, 1744.
- 24 L. Zhou, X. Kong, M. Gao, F. Lian, B. Li, Z. Zhou and H. Cao, *Inorg. Chem.*, 2014, **53**, 9228.
- 25 L. Shao, J. Shu, R. Ma, M. Shui, L. Hou, K. Wu, D. Wang and Y. Ren, *Int. J. Electrochem. Sci.*, 2013, **8**, 1170.
- 26 W. Kang, D. Y. W. Yu, W. Li, Z. Zhang, X. Yang, D.-W. Ng, R. Zou, Y. Tang, W. Zhang and C.-S. Lee, *Nanoscale*, 2015, **7**, 10146.
- 27 Z. Cao, Y. Ding, J. Zhang, Q. Wang, Z. Shi, N. Huo and S. Yang, *RSC Adv.*, 2015, **5**, 56299.
- 28 L. Zhang, T. Mei, X. Wang, J. Wang, J. Li, W. Xiong, Y. Chen and M. Hao, *CrystEngComm*, 2015, **17**, 6450.
- 29 Y. Zhong, M. Yang, X. Zhou, Y. Luo, J. Wei and Z. Zhou, *Adv. Mater.*, 2015, **27**, 806.
- 30 F. Zhang, R. Zhang, G. Liang, J. Feng, L. Lu and Y. Qian, *Mater. Lett.*, 2013, **111**, 165.
- 31 M. Aragon, B. Leon, C. Vicente and J. Tirado, *J. Power Sources*, 2011, **196**, 2863.
- 32 S. Mirhashemihaghighi, B. Leon, C. Vicente, J. Tirado, R. Stoyanova, M. Yoncheva, E. Zhecheva, R. Puche, E. Arroyo and J. de Paz, *Inorg. Chem.*, 2012, **51**, 5554.
- 33 Y. Yan, Y. Zhu, Y. Yu, J. Li, T. Mei, Z. Ju and Y. Qian, *J. Nanosci. Nanotechnol.*, 2012, **12**, 7334.
- 34 S. Wu, R. Xu, M. Lu, R. Ge, J. Iocozzia, C. Han, B. Jiang and Z. Lin, *Adv. Energy Mater.*, 2015, 201500400.
- 35 J. Jamnik and J. Maier, *Phys. Chem. Chem. Phys.*, 2003, **5**, 5215.
- 36 J. Shin, D. Samuelis and J. Maier, *Adv. Funct. Mater.*, 2011, **21**, 3464.
- 37 P. Balaya, *Energy Environ. Sci.*, 2008, **1**, 645.
- 38 Y. Zhukovskii, P. Balaya, E. Kotomin and J. Maier, *Phys. Rev. Lett.*, 2006, **96**, 058302.
- 39 B. Shin, Y. Nam, J. Kim, Y. Lee and Y. Jung, *Sci. Rep.*, 2014, **4**, 5572.
- 40 Yu. F. Zhukovskii, E. A. Kotomin, P. Balaya and J. Maier, *Solid State Sci.*, 2008, **10**, 491.
- 41 R. Liu, S. Zhao, M. Zhang, F. Feng and Q. Shen, *Chem. Commun.*, 2015, **51**, 5728.
- 42 W. Kang, Y. Tang, W. Li, X. Yang, H. Xue, Q. Yang and C. Lee, *Nanoscale*, 2015, **7**, 225.
- 43 J. Maier, *Nat. Mater.*, 2005, **4**, 805.
- 44 Y. Sun, X. Hu, W. Luo, F. Xia and Y. Huang, *Adv. Funct. Mater.*, 2013, **23**, 2436.
- 45 F. Feng, W. Kang, F. Yu, H. Zhang and Q. Shen, *J. Power Sources*, 2015, **282**, 109.
- 46 H. Su, Y. Xu, S. Feng, Z. Wu, X. Sun, C. Shen, J. Wang, J. Li, L. Huang and S. Sun, *ACS Appl. Mater. Interfaces*, 2015, **7**, 8488.
- 47 Q. Li, L. Yin, Z. Li, X. Wang, Y. Qi and J. Ma, *ACS Appl. Mater. Interfaces*, 2013, **5**, 10975.
- 48 H. Wang, L. Cui, Y. Yang, H. Sanchez Casalongue, J. Robinson, Y. Liang, Y. Cui and H. Dai, *J. Am. Chem. Soc.*, 2010, **132**, 13978.
- 49 J. Guo, Q. Liu, C. Wang and M. Zachariah, *Adv. Funct. Mater.*, 2012, **22**, 803.
- 50 E. Liu, J. Wang, C. Shi, N. Zhao, C. He, J. Li and J. Jiang, *ACS Appl. Mater. Interfaces*, 2014, **6**, 18147.